Heliyon 10 (2024) e28068

Contents lists available at ScienceDirect

Heliyon

journal homepage: www.cell.com/heliyon

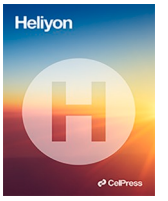

Research article

# Targeting optimal power consumption: Optimizing operational parameters for orchard furrowing and fertilizing machine

Hongjian Zhang [a,b,1], Shuai Fan [a,1], Zixu Chen [a], Xin Han [a], Linlin Sun [a,b], Jingwei Sun [a], Guangming Wang [a,c], Shenghui Fu [a], Chengfu Zhang [d], Jinxing Wang [a,c,*], Shuangxi Liu [a,b,**]

[a] College of Mechanical and Electronic Engineering, Shandong Agricultural University, Taian, Shandong, 271018, China
[b] Shandong Province Key Laboratory of Horticultural Machinery and Equipment, Taian, Shandong, 271018, China
[c] Shandong Provincial Engineering Laboratory of Agricultural Equipment Intelligence, Taian, Shandong, 271018, China
[d] Gaomi Yifeng Machinery Corporation, Gaomi, Shandong, 261500, China

ARTICLE INFO

*Keywords:*
Optimal power consumption
Furrowing device
Orchard furrowing and fertilizing machine
Operational parameters

ABSTRACT

In response to the problem of excessive power consumption during the furrowing operation of orchard furrowing fertilizer machines, an optimization experiment of furrowing operation parameters for orchard furrowing fertilizer machine was conducted based on discrete element simulations. This research focused on the impact of furrowing device operation parameters on furrowing power consumption under full machine operating conditions. Firstly, a kinematics analysis of the soil granules during cutting was done. The mathematical model of soil granules through three movement processes of rising, detachment, and falling was established to determine the main factors affecting the power consumption of furrowing. Secondly, in assessing the furrowing power consumption, the stability coefficient of the furrowing depth, and the percentage of soil cover, alongside the key parameters of furrowing depth, forward propulsion velocity, and furrowing blade rotation speed, a comprehensive quadratic orthogonal rotation regression experiment was meticulously conducted. It was established that test metrics and test parameters regress. Finally, the test parameters were comprehensively optimized after analyzing each factor's impact on the test metrics. The orchard furrowing fertilizer machine's optimal operating parameters were determined, and the verification test was performed. According to the field test findings, the forward propulsion velocity was 785 m/h, and the furrowing blade rotation speed was 190 r/min when the furrowing depth was 275 mm. At this point, the furrowing power consumption was 2.39 kW, the soil cover percentage was 69.06%, and the furrowing depth stability coefficient was 95.08%. These results were in line with the requirements of orchard furrowing operation. The findings of the study can be utilized as a guide for structural changes to orchard furrowing equipment and the management of furrowing operation parameters.

* Corresponding author. College of Mechanical and Electronic Engineering, Shandong Agricultural University, Taian, Shandong, 271018, China.
** Corresponding author. College of Mechanical and Electronic Engineering, Shandong Agricultural University, Taian, Shandong, 271018, China.
*E-mail addresses:* jinxingw@163.com (J. Wang), shuangxiliu168@163.com (S. Liu).
[1] These two authors contributed equally to this work.

https://doi.org/10.1016/j.heliyon.2024.e28068
Received 4 January 2024; Received in revised form 12 February 2024; Accepted 11 March 2024
Available online 15 March 2024

## 1. Introduction

With the largest area of fruit tree plantations and the highest yield of fruit production globally, China leads in both fruit production and consumption [1]. Fruit plantations covered 12,808 thousand hectares and yielded 299.702 million tons of fruit in 2021, respectively. China's mechanized management of orchards has seen gradual improvements in recent years. There has been considerable advancement in the technology and equipment employed for orchard furrowing and fertilization, making them an area of focus for industry research [2,25,27]. Orchard furrowing-fertilizer machines are capable of completing the processes of furrowing, fertilizing, and soil covering in a single operation [3]. Compared to traditional manual furrowing and fertilization in orchards, fruit orchard trenching and fertilizing machines offer advantages such as higher efficiency, lower costs, and improved fertilization effectiveness. However, due to the complex structure and harsh working environment of orchard furrowing and fertilizing machines, as well as the significant variations in the composition of basic fertilizer and soil materials and their properties, along with diverse movement characteristics, it results in excessive power consumption during furrowing operations, directly affecting the quality of orchard trenching work and fruiter yields [4,5]. Therefore, accurately predicting the power consumption during furrowing is of significant importance.

In recent years, the analysis and optimization of energy consumption of agricultural machinery has become a research hotspot. Researchers investigated various aspects, including the structure of furrowing equipment, the characteristics of soil movement, and the laws governing the impact of power consumption in furrowing. Their objective was to improve the efficiency of energy utilization during furrowing operations [6–8]. Qin et al. [9] conducted research on the innovative aspects of trenching blade technology, leading to the development of an energy-efficient trenching blade design. This innovation not only reduces the power consumption during operation but also ensures the effectiveness of the furrowing process. Similarly, Wang et al. [10] have developed a furrowing component specifically for a mountain orchard furrowing machine. The authors investigated how operational parameters affect furrowing energy consumption and used simulations to optimize the furrowing blade's structural properties. The gang angle, furrowing depth and forward propulsion velocity all impact power usage when furrowing. Power usage decreases as the tilt angle increases and remains relatively stable when the furrowing cutterhead diameter changes [11]. With an escalation in rotational speed, the mean power consumption, peak power consumption, and specific energy demands of distinct geometric furrowing blades exhibit a remarkable rise, particularly beyond 375 rpm [12]. Diverse speeds have differing impacts on the quantity of soil pressure and disturbance that furrowing machines create. Barr et al. [13] state that raising the forward propulsion velocity of furrowing machines can decrease soil disturbance.

Ma et al. [14] conducted a study on the impact of forward speed, disc speed, and disc combination on the operational power consumption of a segmented furrow-opening device. They observed that the influence on furrow-opening operational power consumption follows the order from most to least significant: forward speed, disc combination, and disc speed. Kang et al. [15] used the Smooth Particle Hydrodynamics method to build a finite element model of the soil-furrowing blade. They used simulation analyses to determine the furrowing blade's power consumption pattern during the dirt cutting procedure. When the furrowing blade first makes contact with the soil, power consumption increases rapidly, with subsequent growth becoming less pronounced. When the furrowing blade finishes cutting and leaves the soil, power consumption decreases rapidly. The power consumption for the furrowing blade in soil cutting exhibits periodic fluctuations [16].

By examining the adhesion and damping of soil granules, Tamás [17] enhanced a soil-furrowing cutter discrete element model for furrowing power prediction. When modeling granular structures, the Discrete Element Method is frequently employed and offers a practical remedy for nonlinear interactions between furrowing components and soil. It makes it possible to gather information that is difficult to collect through field tests, making it easier to evaluate the effectiveness of furrowing components [18].

The features of orchard furrowing procedures typically impact the depth of the furrow, forward propulsion velocity, and soil cutting speed, which in turn affects the power consumption of the furrowing operations, as per a review of domestic and international research. The objective of this study is to fulfil the job requirements while optimizing power efficiency during furrowing operations. Parameter optimization experiments were diligently undertaken through the utilization of a self-designed orchard furrowing and

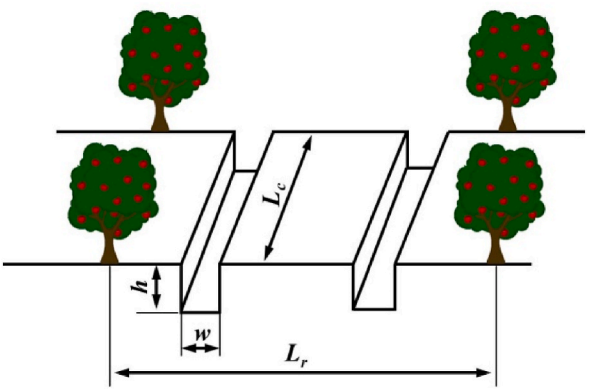


**Fig. 1.** Planting model of modern orchard.

fertilization apparatus, constructed upon the framework of discrete element simulation. These investigations sought to unveil the intricate interplay between the operational parameters of furrowing and their impact on power consumption.

## 2. Material and methods

### 2.1. Agronomic requirements and machine structure

#### 2.1.1. Agronomic requirements for furrowing and fertilizing orchards

Currently, in regions such as the Bohai Bay and the North-Western Loess Plateau, the newly established modern orchards predominantly employ the planting method of dwarf rootstock densely planted, as illustrated in Fig. 1. The modern orchards feature an inter-row spacing, denoted as Lr, ranging from 3.5 to 4.0 m, and an intra-row spacing, denoted as Lc, ranging from 1 to 1.2 m. The fruit trees are commonly pruned into a high spindle tree shape, providing ample space for inter-row operations and facilitating mechanized tasks. To promote shoot growth, flowering, and fruiting of the trees, it is customary to apply deep basal fertilization in trenches dug just below the outer edge of the tree crown during autumn.

#### 2.1.2. Machine structure

Incorporating the high-density planting model for fruit trees, an orchard furrowing-fertilizer machine has been designed, and its overall structure is illustrated in Fig. 2. The machine primarily consists of a frame, fertilizer tank, furrowing device, fertilizer discharge unit, and control system, with key technical specifications outlined in Table 1.

### 2.2. Optimization research methodology for operation parameters

To obtain the optimal combination of operational parameters that meets agronomic requirements while achieving the lowest furrowing power consumption, a systematic approach was employed. Firstly, a theoretical discussion and analysis of the furrowing process were conducted to identify the key factors influencing operational efficiency. Secondly, the discrete element method was applied to simulate and analyze the operation process of the furrowing device. Subsequently, using the Central Composite experimental design methodology, a second-order orthogonal rotation regression experiment was conducted to establish a regression mathematical model. Based on this, a comprehensive exploration of the impact of operational parameters on furrowing power consumption for the orchard furrowing fertilizer machine was conducted, investigating the influence of test parameters on the test metrics. Finally, field experiments were conducted to further validate the accuracy of the research results, as depicted in Fig. 3.

## 3. Results and discussion

### 3.1. Kinematic analysis of soil granules

Delving into the kinematic characteristics of soil granules during cutting serves as an essential foundation for a comprehensive inquiry into critical factors, including the furrowing power consumption, the stability coefficient of the furrowing depth, and the percentage of soil cover. When the furrowing machine is in operation, the furrowing blade enters the soil, leading to three fundamental motion phases for soil granules: ascent, detachment, and descent. During the detachment and descent phases, these particles may undergo two main types of motion. One scenario involves the occurrence of a collision-fall process, in which particles collide with the soil-covering hood after impact and then return to the furrow. Another scenario is the direct-fall process, where particles do not come into contact with the soil-covering hood but instead fall directly into the furrow.

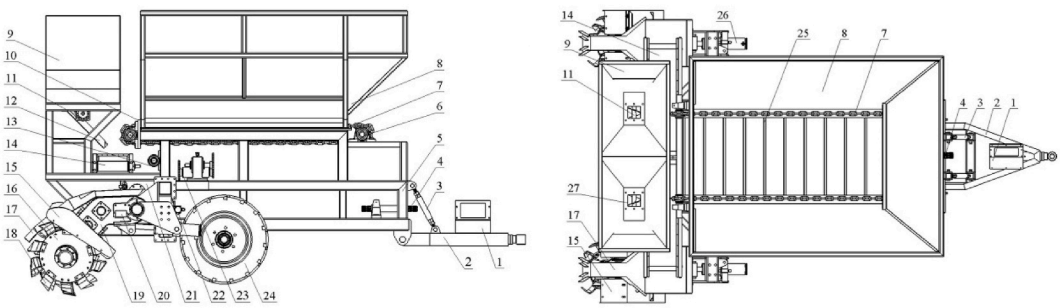


**Fig. 2.** Structure diagram of orchard furrowing-fertilizer machine.
Note: 1. Control box 2. Traction frame 3. Adjust the pull tube 4. Transmission shaft 5. Rack 6. Fertilizer sprocket 7. Looped chain 8. Organic fertilizer bin 9. Fertilizer bin 10. Organic fertilizer distribution outlet 11. Fertilizer worm conveyor 12. Fertilizer conveyor disc 13. Fertilizer transmission bin 14. Fertilizer material handling belt 15. Soil-covering hood 16. Furrowing cutterhead 17. Fertilizer guide plate 18. Furrowing blade 19. Furrowing transmission box 20. Angle sensor 21. Main transmission box 22. Lateral hydraulic cylinder 23. Fertilizer transmission box 24. Wheels 25. Fertilizing scraper 26. Longitudinal hydraulic cylinder 27. Fertilizer discharge port.

**Table 1**
Main technical parameters.

| Parameter | Numerical Value |
|---|---|
| Matching power/kW | ≥58.8 |
| Operating speed/(m·s$^{-1}$) | 0.4–1.2 |
| Machine dimensions (length × width × height)/(mm × mm × mm) | 4030 × 2470 × 2150 |
| Furrowing depth/mm | 0–400 |
| Furrow width/mm | 150–350 |
| Furrow interval adjustment range/mm | 2000–2600 |
| Furrow blade rotation speed/(r•min$^{-1}$) | 0–230 |
| Furrowing cutterhead diameter/mm | 300 |
| Organic fertilizer box capacity/L | 2450 |
| Fertilizer bin volume/L | 650 |

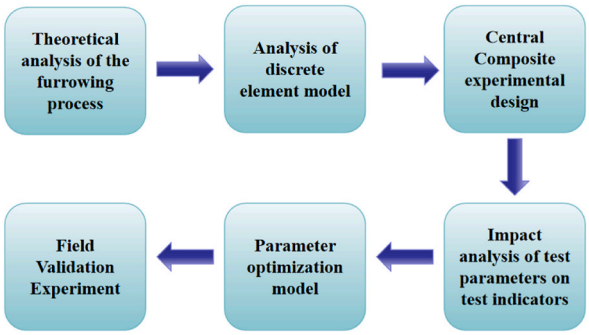


**Fig. 3.** Optimization research methodology for operation parameters.

*3.1.1. Kinematic analysis of the ascending process of soil granules*

During the rising process, soil granules adhere to the furrowing blade and rotate along with it. When the centrifugal force acting on the soil granules surpasses the adhesive force, they detach from the furrowing blade and undergo parabolic motion. Some of the detached particles collide with the soil-covering hood and fall back into the furrow, while others directly fall back into the furrow. Throughout the process in which the soil granules have not detached from the furrowing blade, we can consider them as a point mass [19]. Kinematic analysis is performed on the soil granules that are about to separate from the furrowing blade, as depicted in Fig. 4.

We have created a planar Cartesian coordinate system in this case, with the origin being the point of intersection between the furrow's base and the trajectory circle of the furrowing blade's endpoint. While the positive *y*-axis extends vertically from the furrow bottom, the positive *x*-axis is oriented in the opposite direction of forward movement. Point *E* represents the furrowing blade's rotational center.

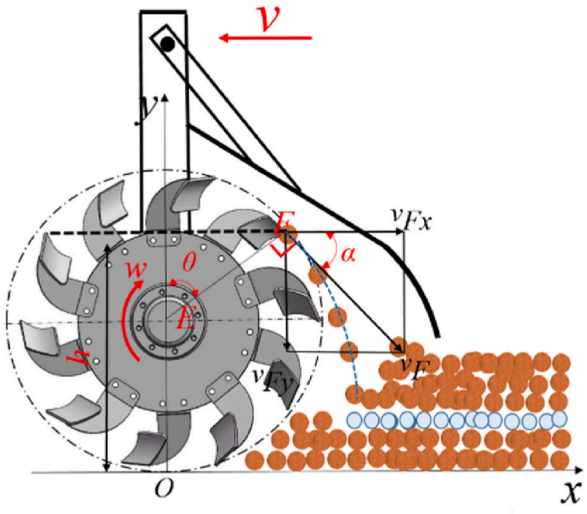


**Fig. 4.** Kinematics model of soil rising process.

Assume for the moment that soil granules begin their parabolic flight at point *F*, the terminal of the furrowing blade. A soil granule's velocity is equal to the absolute velocity of the furrowing blade's endpoint at point *F* right before it separates from it. This indicates that the soil granule's velocity at point *F* exactly matches the furrowing blade's endpoint's velocity at that same place. As a result, the soil granule's motion speed at point *F* is:

$$\begin{cases} v_F = \sqrt{v_{Fx}^2 + v_{Fy}^2} = \sqrt{v_m^2 - 2v_m w R_1 \sin wt + w^2 R_1^2} \\ \theta = \alpha = \cos^{-1}\left(\dfrac{h - R_1}{R_1}\right) \end{cases} \tag{1}$$

In the context of our study, we define the following variables: '*h*' signifies the vertical displacement from the terminus '*F*' of the furrowing blade to the base of the furrow, measured in m; '$R_1$' designates the radial span at the endpoint of the furrowing blade, expressed in m; '$\alpha$' denotes the azimuthal angle, measured in rad, representing the angular displacement between the horizontal velocity vector and the absolute velocity vector at the terminus '*F*' of the furrowing blade; '$\theta$' represents the inclination angle, also in rad, characterizing the angular deviation between the trajectory of point '*F*' in the normal direction and the *y*-axis; '$\omega$' encapsulates the angular velocity governing the rotation of the furrowing blade, measured in rad/s; '$v_m$' designates the linear velocity of the entire apparatus as it advances, expressed in m/s; '$v_{Fx}$' portrays the vector component of soil granule velocity at point '*F*' along the *x*-axis, in m/s; '$v_{Fy}$' delineates the vector component of soil granule velocity at point '*F*' along the *y*-axis, similarly in m/s; '*t*' represents the temporal duration of the furrowing blade's operation, measured in seconds; lastly, '$v_F$' stands for the scalar magnitude of soil granule velocity at point '*F*', expressed in m/s.

### *3.1.2. Kinematic analysis of the collision and falling process of soil granules*

When soil granules move to the soil-covering hood, they collide with the hood, causing their motion speed and direction to change and bounce, before falling back into the furrow. In our endeavor to scrutinize the intricate motion of soil granules following their collision, we designate the point of collision, $O_1$, as the initial reference point. Subsequently, we institute an immobile coordinate framework, denoted as $O_1x_1y_1$. Upon the particle's resilient rebound, we institute a dynamic coordinate system, christened $O_2x_2y_2$, whose origin harmonizes with the center of mass of the soil granule. Herein, the normal and tangent aspects of the particle's trajectory are aligned with the horizontal and vertical axes, respectively [20], as visually depicted in Fig. 5.

In our study, '$\beta_1$' designates the angle of approach, expressed in °, which characterizes the inclination of soil granules before their encounter with the soil-covering hood. Meanwhile, '$\beta_2$' signifies the angle of deflection, also measured in °, marking the change in trajectory following the interaction between the soil granules and the soil-covering hood.

Following the collision, the soil granules initiate a complex spatial motion. We postulate several assumptions regarding the behavior of soil granules after this collision event: Firstly, the trajectory of soil granules post-rebound is constrained to the same plane as their initial falling path. Secondly, any intrinsic rotation of the soil granules themselves is considered negligible in our analysis. Thirdly, it is assumed that the rebound angle '$\beta_2$' of the soil granules, subsequent to the collision, maintains an equivalence in magnitude to the angle of incidence, '$\beta_1$'.

Under the aforementioned assumptions, the soil granules, after the collision, continue their movement under the influence of gravity and air resistance, until they fall back into the furrow. During the entire collision-fall motion process, the air resistance experienced by the soil granules is:

$$F_R = mgf(v) \tag{2}$$

Within the equation, '$F_R$' stands for the aerodynamic resistance, measured in N; 'm' signifies the mass of the soil granules, expressed

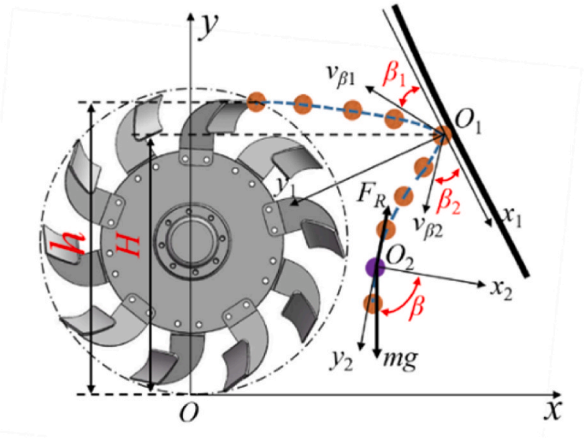


**Fig. 5.** Kinematics model of the soil collision falling process.

in kg; and 'g' denotes the gravitational acceleration, set at 9.8 m/s$^2$.

$F(v)$ represents the function relation with the velocity under air resistance. In the formula:

$$f(v_0) \geq 0 \tag{3}$$

During the collision-fall process, the trajectory equation and velocity equation of the soil granules are as follows:

$$S_1 = S_1(t) \tag{4}$$

$$v_1 = \frac{dS_1}{dt} \tag{5}$$

$$\begin{cases} m\dfrac{dv_1}{dt} = mg\sin\beta - mgf(v_1) \\ m\dfrac{v_1^2}{r} = mg\cos\beta \end{cases} \tag{6}$$

Within this mathematical expression, '$S_1$' is representative of the displacement trajectory of soil granules throughout the collision-fall process, denominated in m; '$v_1$' delineates the velocity of motion exhibited by the soil granules during this particular sequence, quantified in m/s; '$r$' pertains to the radius of curvature characterizing the trajectory that soil granules follow during the collision-fall event, measured in mm; and '$\beta$' designates the angular deviation between the mobile coordinate system, referred to as '$O_2x_2$,' and the vertical downward orientation, articulated in °. In the formula:

$$\beta = \beta(t) \tag{7}$$

This allows us to obtain the differential equation for the soil granule center of mass in the moving coordinate system, which is as follows:

$$\frac{dv_1}{d\beta} = v_1\tan\beta - \frac{v_1 f(v_1)}{\cos\beta} \tag{8}$$

The initial conditions are as follows:

$$v_{\beta 2} = \lambda v_{\beta 1} \tag{9}$$

In this equation, '$v_{\beta 2}$' designates the initial velocity of the soil granules following the collision rebound, expressed in m/s; 'λ' represents collision restitution coefficient; and '$v_{\beta 1}$' signifies the incident velocity, also measured in m/s.

From equations (6)–(9), the trajectory equation for the center of mass $(x_1, y_1)$ of soil granules in the fixed coordinate system $O_1x_1y_1$ during the collision-fall process can be obtained as follows:

$$\begin{cases} x_1 = \dfrac{1}{g}\displaystyle\int_{\beta}^{\beta_2}\left[g\cos\beta\frac{v_1\cos\beta\tan\beta dt - v_1 f(v_1)dt}{\cos\beta dv_1}\right]^2 d\beta \\ y_1 = \dfrac{1}{g}\displaystyle\int_{\beta}^{\beta_2}\left[g\cos\beta\frac{v_1\cos\beta\tan\beta dt - v_1 f(v_1)dt}{\cos\beta dv_1}\right]^2 \tan\beta d\beta \end{cases} \tag{10}$$

In this formula, '$x_1$' denotes the spatial displacement along the '$O_1x_1$' direction of the soil granules during the collision-fall sequence,

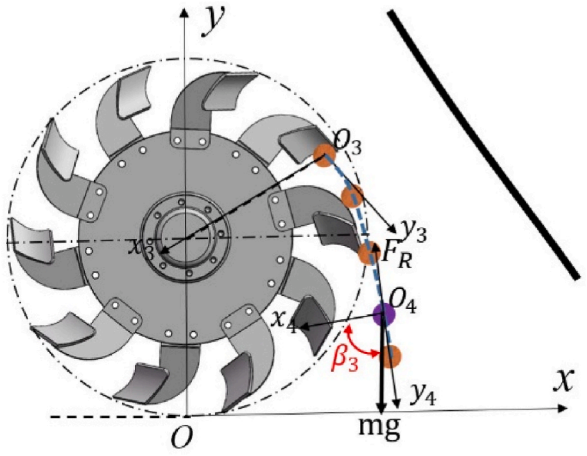


**Fig. 6.** Kinematics model of the soil direct falling process.

measured in m. Similarly, '$y_1$' represents the displacement along the '$O_1y_1$' direction of the soil granules during the same collision-fall process, also quantified in m.

The factors influencing the movement of soil granules during the collision-fall process are as follows, as shown by equation (10): the motion speed $v_1$ of the soil granules during the collision-fall process, the angle $\beta$ between the moving coordinate system $O_2x_2$ axis and the downward vertical direction, and the rebound angle $\beta_2$ after the soil granules collide with the soil-covering hood. These include $\beta$ and $\beta_2$, which correspond to the angle of incidence $\beta_1$ prior to the soil particle collision and the particle speed $v_F$ upon detaching from the furrowing blade, whereas $v_1$ is associated with the incident speed $v_{\beta 1}$. The furrowing depth, forward propulsion velocity, and furrowing blade rotation speed of the furrowing-fertilizer machine in orchards actually affect the incident speed $v_{\beta 1}$ and the speed $v_F$ at which the soil granules detach from the furrowing blade. This, in turn, influences the motion state of the soil granules and the operation effect.

### 3.1.3. Kinematic analysis of the direct falling process of soil granules

After detaching from the furrowing blade, some soil granules, under the joint action of gravity and air resistance, do not collide with the soil-covering hood and continue to follow a parabolic trajectory falling back into the furrow. In our pursuit of unraveling the intricacies governing the descent of soil granules, we instantiate an immutable reference frame designated as $O_3x_3y_3$. Within this system, the point of origin, $O_2$, coincides with the initial location of soil granule detachment from the furrowing blade. Following detachment, we introduce a dynamic coordinate system, christened $O_4x_4y_4$, in which the center of mass of the soil granules is established as the origin. Herein, the normal and tangent aspects of the particle's trajectory are aligned with the horizontal and vertical axes, respectively, as visually depicted in Fig. 6.

The trajectory equation and velocity equation for the motion of soil granules during the direct-fall process, as follows:

$$S_2 = S_2(t) \tag{11}$$

$$v_2 = \frac{dS_2}{dt} \tag{12}$$

Within these equations, denoted as '$S_2$' represents the trajectory of soil granules in their direct descent, measured in m, and '$v_2$' signifies the velocity of these soil granules during their direct descent process, expressed in m/s.

The forces of gravity and air resistance acting on the soil granules are separately projected under the moving coordinate system, as shown in formula (13).

$$\begin{cases} m\dfrac{dv_2}{dt} = mg\sin\beta_3 - mgf(v_2) \\ m\dfrac{v_2^2}{\rho} = mg\cos\beta_3 \end{cases} \tag{13}$$

Within this equation, '$\rho$' denotes the radius of curvature characterizing the trajectory during the direct-fall sequence of the soil granules, measured in m. Meanwhile, '$\beta_3$' represents the angular deviation between the axis of the mobile coordinate system '$O_4x_4$' and the vertical downward orientation, expressed in °. In the formula:

$$\rho = \rho(t) \tag{14}$$

$$\beta_3 = \beta_3(t) \tag{15}$$

This allows us to determine the differential equation for the location of the soil granule center of mass inside the dynamic coordinate system, which is as follows:

$$\frac{dv_2}{d\beta_3} = v_2\tan\beta_3 - \frac{v_2 f(v_2)}{\cos\beta_3} \tag{16}$$

The initial conditions are as follows:

$$v_{o3} = v_F = \sqrt{v_m^2 - 2v_m w R_1\sin wt + w^2R_1^2} \tag{17}$$

$$\beta_0 = \alpha = \cos^{-1}\left(\frac{h - R_1}{R_1}\right) \tag{18}$$

In this equation, $v_{o3}$ denotes the inaugural velocity of soil granules upon their emancipation from the furrowing blade, measured in m/s; while $\beta_0$ characterizes the angular deviation between the velocity vector at the point of soil granule detachment and the $x$-axis, also measured in °.

From formulas (13) to (18), the trajectory equation of the center of mass ($x_2$, $y_2$) of the soil granules in the fixed coordinate system $O_3x_3y_3$ during the direct-fall process can be obtained as follows:

$$\begin{cases} x_2 = \dfrac{1}{g}\displaystyle\int_{\beta_0}^{\beta_3}\left[g\cos\beta_3\dfrac{v_2\cos\beta_3\tan\beta_3 dt - v_2 f(v_2)dt}{\cos\beta_3 dv_3}\right]^2 d\beta_3 \\ y_2 = \dfrac{1}{g}\displaystyle\int_{\beta_0}^{\beta_3}\left[g\cos\beta_3\dfrac{v_2\cos\beta_3\tan\beta_3 dt - v_2 f(v_2)dt}{\cos\beta_3 dv_3}\right]^2 \tan\beta_3 d\beta_3 \end{cases} \tag{19}$$

In this equation, $x_2$ signifies the displacement along the $O_3x_3$ axis as the soil granules directly descend, measured in m, while $y_2$ represents the displacement along the $O_3y_3$ axis, as these particles directly navigate their direct descent, also measured in m.

The factors influencing the movement of soil granules during the direct-fall process are as follows, as shown by equation (19): angle $\beta_0$, representing the angular deviation between the velocity vector at the point of particle detachment and the $x$-axis; angle $\beta_3$, delineating the angle between the moving coordinate system $O_4x_4$ axis and the downward vertical direction; and the translational velocity, denoted as $v_2$, at which the soil granules engage in their direct descent. Among these, $\beta_0$ and $\beta_3$ are related to the speed $v_F$ of the soil granules when they detach from the furrowing blade and the furrowing depth $h$, while $v_2$ is related to the speed $v_F$ of the soil granules when they detach from the furrowing blade. In the actual operation of the furrowing-fertilizer machine in orchards, its furrowing depth, forward propulsion velocity, and furrowing blade rotation speed influence the speed $v_F$ at which the soil granules detach from the furrowing blade and the incident speed $v_{\beta 1}$. Consequently, this in turn exerts an influence on the dynamic state of the soil granules and, in extension, the efficacy of the operational outcome.

Through a comprehensive analysis of the entire motion process of soil granules, we have found that the depth of furrowing, forward propulsion velocity, and the rotation speed of the furrowing blade significantly affect the motion state of soil granules, thereby influencing the furrowing power consumption, the stability coefficient of the furrowing depth, and the percentage of soil cover. Therefore, the following sections will use EDEM discrete element simulation and the Central Composite experimental method to study the influence of furrowing depth, forward propulsion velocity, and rotation speed of the furrowing blade on furrowing power consumption.

### 3.2. Analysis and experimentation of discrete element model

#### 3.2.1. Establishment of discrete element model

For increased simulation accuracy, the furrowing tool was entered into the EDEM simulation program at its original size. As a

**Table 2**
EDEM simulation parameters of furrowing operation.

| Material | Parameter | Value | Source |
|---|---|---|---|
| Tilled layer soil | Density/kg·m$^{-3}$ | 1669 | Measurement |
| | Poisson's ratio | 0.40 | Literature |
| | Shear modulus/MPa | 1.0 | Literature |
| Plow bottom layer soil | Density/kg·m$^{-3}$ | 1956 | Measurement |
| | Poisson's ratio | 0.42 | Literature |
| | Shear modulus/MPa | 1.3 | Literature |
| Core soil layer soil | Density/kg·m$^{-3}$ | 1755 | Measurement |
| | Poisson's ratio | 0.40 | Literature |
| | Shear modulus/MPa | 1.1 | Literature |
| 65Mn | Density/kg·m$^{-3}$ | 7.82 × 103 | Literature |
| | Poisson's ratio | 0.29 | |
| | Shear modulus/MPa | 8.19 × 104 | |
| 65Mn-Tilled layer soil | Restitution coefficient | 0.6 | Literature |
| | Static friction coefficient | 0.5 | Measurement |
| | Kinetic friction coefficient | 0.11 | Measurement |
| 65Mn-Plow bottom layer soil | Restitution coefficient | 0.6 | Literature |
| | Static friction coefficient | 0.5 | Measurement |
| | Kinetic friction coefficient | 0.13 | Measurement |
| 65Mn-Core soil layer soil | Restitution coefficient | 0.6 | Literature |
| | Static friction coefficient | 0.5 | Measurement |
| | Kinetic friction coefficient | 0.08 | Measurement |
| Tilled layer soil-Tilled layer soil | Restitution coefficient | 0.6 | Literature |
| | Static friction coefficient | 0.4 | Measurement |
| | Kinetic friction coefficient | 0.15 | Measurement |
| | JKR/J·m$^{-2}$ | 2.3 | Experimental calibration |
| Plow bottom layer soil-Plow bottom layer soil | Restitution coefficient | 0.6 | Literature |
| | Static friction coefficient | 0.4 | Measurement |
| | Kinetic friction coefficient | 0.20 | Measurement |
| | JKR/J·m$^{-2}$ | 6.0 | Experimental calibration |
| Core soil layer soil-Core soil layer soil | Restitution coefficient | 0.6 | Literature |
| | Static friction coefficient | 0.4 | Measurement |
| | Kinetic friction coefficient | 0.18 | Measurement |
| | JKR/J·m$^{-2}$ | 4.1 | Experimental calibration |

result, a soil trough, characterized by dimensions of 3000 mm in length, 800 mm in width, and 400 mm in thickness, was generated using EDEM software. This model was created in line with the simulation parameters presented in Table 2 [[26],21], which were derived from the soil stratification theory and factors such as the furrowing device's overall size and operation parameters, depicted in Fig. 7. The built-in soil trough's thickness and cross-sectional layout matched the real properties of the orchard soil. The soil granule units' radius in each layer measured 8 mm. The tilled soil layer was 150 mm, the plow bottom soil layer was 100 mm, and the core soil layer was 150 mm thick.

#### 3.2.2. Calculation of furrowing power consumption

In accordance with the method of evaluating the quality of furrowing machine operation stipulated in NY/T740-2003, combined with the performance requirements during field operations, the furrowing power consumption was selected as the indicator for evaluating the operation effect. The following is the formula for calculating power:

$$P = \frac{T \times n}{9550\eta} \tag{20}$$

In this formula, '$P$' signifies the power consumption attributed to the furrowing process, quantified in kilowatts; '$T$' pertains to the torque measured in the course of testing, expressed in Newton-meters; '$n$' designates the rotational speed of the furrowing blade during the testing phase, measured in revolutions per minute (r/min); and '$\eta$' represents the coefficient of transmission efficiency, a value assumed to be 0.9.

#### 3.2.3. Preliminary experiment simulation process and analysis

The following settings were made for the EDEM software's Creator module: 300 mm of furrowing depth, 700 m/h of forward motion, and a direction parallel to the furrowing device's forward motion. The furrowing blade was programmed to rotate around the positive Y-axis at 190 r/min in a clockwise orientation. In the EDEM software Simulator module, the subsequent parameters were configured as follows: the temporal increment was established at 17% (equivalent to $1.85 \times 10^{-4}$ s), the period of action was designated as 18.6 s, the time interval for data preservation was set at 0.05 s, and the grid unit dimensions were specified to be double the minimum radius of the soil granules. A pre-test was performed for a particular operating state to better evaluate the effect of the furrowing device's operational parameters on its performance. This is illustrated in Fig. 8.

Upon the conclusion of the experimental procedure, an array of measurements and statistical analyses was undertaken utilizing the EDEM software Analyst module, as illustrated in Fig. 9. These assessments encompassed the analysis of furrowing blade torque, furrowing depth, and the number of covered particles. In the course of that procedure, it was necessary to measure the torque when the furrowing blade was fully placed in the soil trench and export the obtained measurement results through the Analyst module. The furrowing depth ($h$) was defined as the straight-line distance from the furrow's bottom line to the ground, where $N_{0i}$ and $N_{1i}$ respectively represented the particle quantities in the measurement area before and after the furrowing operation. Assessment indicators were then calculated for each operation effect. The values for furrowing power consumption ($y_1$), furrowing depth stability coefficient ($y_2$), and soil cover percentage ($y_3$) were 3.60 kW, 98.07%, and 81.41%, respectively.

Single-factor simulation experiments were conducted with furrowing power consumption ($y_1$), furrowing depth stability coefficient ($y_2$), and soil coverage rate ($y_3$) as the experimental indicators. The value ranges for each experimental factor were determined based on the theoretical analysis of the furrow-opening device of the orchard double-row fertilizing machine, relevant agronomic requirements, and the results of the single-factor simulation experiments, as detailed in Table 3.

### 3.3. Predictive model for orchard furrowing power consumption

#### 3.3.1. Experimental design

The study employed the Central Composite experimental design methodology to examine the interactive effects and influence patterns of three parameters, namely furrowing depth, forward propulsion velocity, and furrowing blade rotation speed, on furrowing power consumption, furrowing depth stability, and soil cover percentage [22]. To ascertain the optimal operational conditions for the orchard furrowing and fertilizer machine, an experimental investigation of operational parameters was meticulously carried out. Following a meticulously planned experimental framework, the independent variables furrowing depth '$h$,' forward propulsion velocity '$v$,' and furrowing blade rotation speed '$n$' were firmly established as '$x_1$,' '$x_2$,' and '$x_3$,' respectively. Response values $y_1$, $y_2$, and

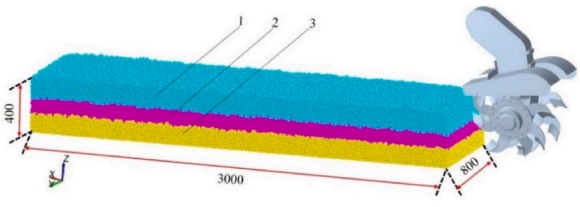


**Fig. 7.** Geometric model of a furrowing mechanism and a soil bin simulation.
Note: 1. Tilled layer 2. Plow bottom layer 3. Core soil layer.

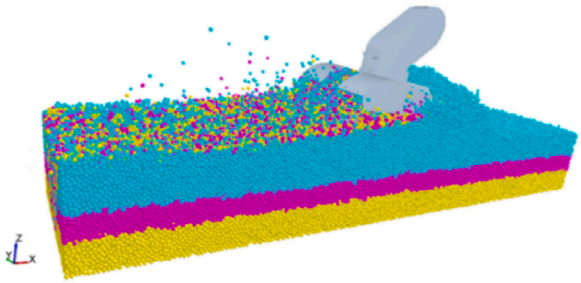

**Fig. 8.** Status of orchard furrowing.

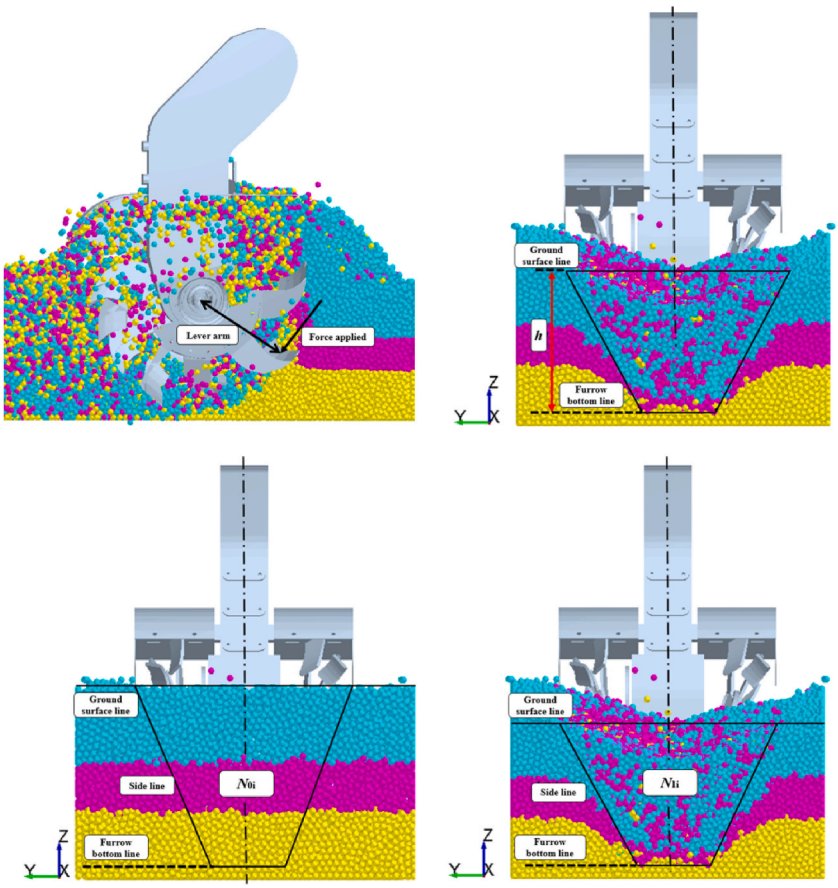


**Fig. 9.** Measuring several indices during a furrowing operation.
Note: The bottom line of the furrow was the fitted straight line at the deepest part of the furrowing, and the side lines were the fitted straight lines on the sides of the furrow profile.

**Table 3**
Test parameters.

| Factors | Value Range |
|---|---|
| Furrowing depth/(mm) | 0–400 |
| Forward propulsion velocity/(m•h$^{-1}$) | 600–1000 |
| Furrowing blade rotation speed/(r•min$^{-1}$) | 180–220 |

**Table 4**
Table of factor sand levels.

| Level | Furrowing Depth $x_1$/(mm) | Forward Propulsion Velocity $x_2$/(m•h$^{-1}$) | Furrowing Blade Rotation Speed $x_3$/(r•min$^{-1}$) |
|---|---|---|---|
| −1.682 | 31.82 | 631.82 | 183.18 |
| −1 | 100 | 700 | 190 |
| 0 | 200 | 800 | 200 |
| 1 | 300 | 900 | 210 |
| 1.682 | 368.18 | 968.18 | 216.82 |

$y_3$ were established for the furrowing power consumption, furrowing depth stability coefficient, and soil cover percentage, respectively. Table 4 displays the creation of a 3-factor, 5-level experimental factor, and encoding level. The outcomes of the orthogonal experiment are displayed in Table 5.

*3.3.2. Establishment of regression model and variance analysis*

The Design-Expert12 program was employed to construct a response surface regression model, encompassing furrowing depth, forward propulsion velocity, and furrowing blade rotation speed, as variables of independent, in relation to the parameters of furrowing power consumption, furrowing depth stability coefficient, and soil cover percentage. The results of the variance analysis, conducted on the regression model, are meticulously detailed in Table 6.

The statistical significance, as elucidated in Table 6, was unmistakably remarkable, with all significance $P$ values pertaining to the models of furrowing power consumption, furrowing depth stability coefficient, and soil cover percentage resting below the 0.05 threshold, illustrating the regression model's high degree of significance. Conversely, the $P$-values associated with the lack of fit item uniformly exceed the 0.05 threshold, signifying the conspicuous absence of factors contributing to model misfit. This, in turn, attests to the model's notably high degree of concordance with the empirical data.

The determination coefficients, '$R^2$,' for the model, were calculated to be 0.9994 for furrowing power consumption, 0.9681 for furrowing depth stability, and 0.9823 for soil cover percentage. These results imply that the model elucidates nearly the entire test result, with only a minimal 0.06%, 3.19%, and 1.77% remaining unexplained, demonstrating an excellent fit and its suitability for experimental prediction.

Regarding the furrowing power consumption model, the regression terms '$x_1$,' '$x_2$,' '$x_3$,' '$x_1x_2$,' '$x_1x_3$,' and '$x_1^2$,' exerted an exceptionally significant influence ($P < 0.01$). In the case of the furrowing depth stability coefficient, the terms '$x_1$,' '$x_1^2$,' and '$x_2^2$' had an exceedingly significant impact ($P < 0.01$), while $x_3$' and '$x_1x_2$' exhibited a significant impact ($P < 0.05$). Lastly, for the soil cover percentage, the terms '$x_1$,' '$x_3$,' and '$x_1^2$' were noted to have an extremely significant impact ($P < 0.01$).

The experiment results in Table 4 underwent to a multi-variable regression fitting analysis using Design-Expert12 software, and the coded second-degree regression model of each factor's impact on furrowing power consumption, furrowing depth stability coefficient, and soil cover percentage was obtained. This model is represented by formulas 21, 22, and 23.

$$y_1 = 1.19 + 1.37x_1 + 0.10x_2 + 0.068x_3 + 0.071x_1x_2 + 0.077x_1x_3 + 9.698E-003x_2x_3 + 0.42{x_1}^2 - 1.253E-003{x_2}^2 + 0.016{x_3}^2 \quad (21)$$

**Table 5**
Experimental design and results of furrowing operation.

| Serial Number | Furrowing Depth | Forward Propulsion Velocity | Furrowing Blade Rotation Speed | Furrowing Power Consumption/kW | Furrowing Depth Stability Coefficient/% | Soil Cover Percentage/% |
|---|---|---|---|---|---|---|
| 1 | 31.82 | 800.00 | 200.00 | 0.0339 | 91.89 | 29.89 |
| 2 | 300.00 | 900.00 | 190.00 | 3.0017 | 98.30 | 75.37 |
| 3 | 200.00 | 968.18 | 200.00 | 1.3525 | 95.62 | 45.72 |
| 4 | 368.18 | 800.00 | 200.00 | 4.6791 | 98.97 | 89.65 |
| 5 | 300.00 | 700.00 | 210.00 | 2.9892 | 97.58 | 74.79 |
| 6 | 200.00 | 631.82 | 200.00 | 0.9787 | 95.81 | 47.63 |
| 7 | 300.00 | 700.00 | 190.00 | 2.6963 | 97.21 | 80.61 |
| 8 | 300.00 | 900.00 | 210.00 | 3.3532 | 98.35 | 70.63 |
| 9 | 100.00 | 900.00 | 210.00 | 0.3235 | 93.70 | 34.2 |
| 10 | 100.00 | 900.00 | 190.00 | 0.2991 | 92.51 | 37.62 |
| 11 | 100.00 | 700.00 | 210.00 | 0.2629 | 94.96 | 34.02 |
| 12 | 200.00 | 800.00 | 183.18 | 1.1396 | 96.60 | 54.27 |
| 13 | 200.00 | 800.00 | 216.82 | 1.2912 | 97.11 | 42.54 |
| 14 | 100.00 | 700.00 | 190.00 | 0.2575 | 92.70 | 38.97 |
| 15 | 200.00 | 800.00 | 200.00 | 1.1566 | 97.93 | 48.57 |
| 16 | 200.00 | 800.00 | 200.00 | 1.1958 | 97.51 | 49.37 |
| 17 | 200.00 | 800.00 | 200.00 | 1.2070 | 96.47 | 50.03 |
| 18 | 200.00 | 800.00 | 200.00 | 1.2048 | 98.28 | 54.73 |
| 19 | 200.00 | 800.00 | 200.00 | 1.2312 | 97.12 | 49.67 |
| 20 | 200.00 | 800.00 | 200.00 | 1.1825 | 97.65 | 50.55 |

**Table 6**
Variance analysis of regression model.

| Evaluation Index | Variance Source | Sum of Squares | Degrees of Freedom | Mean Square | *F* | *P* |
|---|---|---|---|---|---|---|
| Furrowing Power Consumption $y_1$/kW | Model | 28.50 | 9 | 3.17 | 1864.69 | <0.0001** |
| | $x_1$ | 25.63 | 1 | 25.63 | 15093.26 | <0.0001** |
| | $x_2$ | 0.14 | 1 | 0.14 | 84.55 | <0.0001** |
| | $x_3$ | 0.063 | 1 | 0.063 | 37.24 | 0.0001** |
| | $x_1x_2$ | 0.040 | 1 | 0.040 | 23.67 | 0.0007** |
| | $x_1x_3$ | 0.047 | 1 | 0.047 | 27.80 | 0.0004** |
| | $x_2x_3$ | 7.525E-004 | 1 | 7.525E-004 | 0.44 | 0.5207 |
| | $x_1^2$ | 2.54 | 1 | 2.54 | 1495.48 | <0.0001** |
| | $x_2^2$ | 2.264E-005 | 1 | 2.264E-005 | 0.013 | 0.9104 |
| | $x_3^2$ | 3.862E-003 | 1 | 3.862E-003 | 2.27 | 0.1625 |
| | Residual | 0.017 | 10 | 1.698E-003 | | |
| | Lack of Fit | 0.014 | 5 | 2.762E-003 | 4.35 | 0.0661 |
| | Pure Error | 3.171E-003 | 5 | 6.343E-004 | | |
| | Total | 28.52 | 19 | | | |
| Furrowing Depth Stability Coefficient $y_2$/% | Model | 82.42 | 9 | 9.16 | 33.72 | <0.0001** |
| | $x_1$ | 63.62 | 1 | 63.62 | 234.29 | <0.0001** |
| | $x_2$ | 5.992E-004 | 1 | 5.992E-004 | 2.206E-003 | 0.9635 |
| | $x_3$ | 1.64 | 1 | 1.64 | 6.03 | 0.0340* |
| | $x_1x_2$ | 1.37 | 1 | 1.37 | 5.04 | 0.0485* |
| | $x_1x_3$ | 1.15 | 1 | 1.15 | 4.23 | 0.0669 |
| | $x_2x_3$ | 0.24 | 1 | 0.24 | 0.89 | 0.3679 |
| | $x_1^2$ | 8.80 | 1 | 8.80 | 32.40 | 0.0002** |
| | $x_2^2$ | 6.68 | 1 | 6.68 | 24.58 | 0.0006** |
| | $x_3^2$ | 1.11 | 1 | 1.11 | 4.09 | 0.0708 |
| | Residual | 2.72 | 10 | 0.27 | | |
| | Lack of Fit | 0.69 | 5 | 0.14 | 0.34 | 0.8669 |
| | Pure Error | 2.02 | 5 | 0.40 | | |
| | Total | 85.14 | 19 | | | |
| Soil Cover Percentage $y_3$/% | Model | 5233.06 | 9 | 581.45 | 61.76 | <0.0001** |
| | $x_1$ | 4839.87 | 1 | 4839.87 | 514.07 | <0.0001** |
| | $x_2$ | 13.91 | 1 | 13.91 | 1.48 | 0.2521 |
| | $x_3$ | 109.42 | 1 | 109.42 | 11.62 | 0.0067** |
| | $x_1x_2$ | 8.47 | 1 | 8.47 | 0.90 | 0.3653 |
| | $x_1x_3$ | 0.60 | 1 | 0.60 | 0.064 | 0.8059 |
| | $x_2x_3$ | 0.85 | 1 | 0.85 | 0.090 | 0.7698 |
| | $x_1^2$ | 247.66 | 1 | 247.66 | 26.30 | 0.0004** |
| | $x_2^2$ | 3.38 | 1 | 3.38 | 0.36 | 0.5624 |
| | $x_3^2$ | 0.23 | 1 | 0.23 | 0.025 | 0.8780 |
| | Residual | 94.15 | 10 | 9.41 | | |
| | Lack of Fit | 70.34 | 5 | 14.07 | 2.95 | 0.1298 |
| | Pure Error | 23.81 | 5 | 4.76 | | |
| | Total | 5327.21 | 19 | | | |

Note: * indicates a significant effect, $P < 0.05$; ** indicates a highly significant effect, $P < 0.01$.

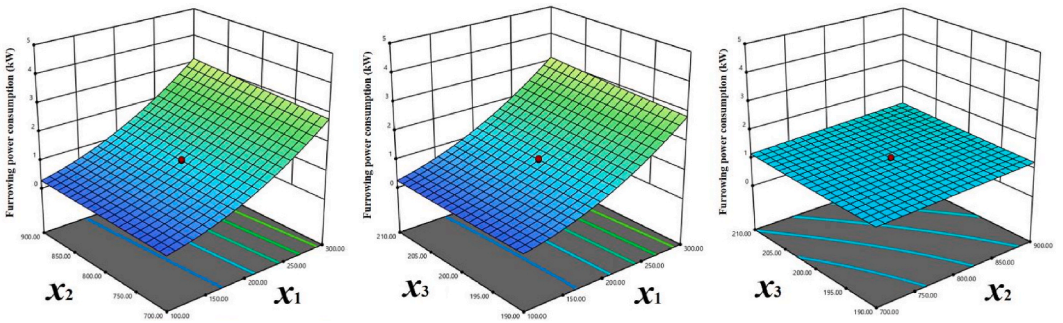


**Fig. 10.** Response surfaces of test factors influence on furrowing power consumption.

$$y_2 = 97.50 + 2.16x_1 + 6.624E - 003x_2 + 0.35x_3 + 0.41x_1x_2 - 0.38x_1x_3 - 0.17x_2x_3 - 0.78{x_1}^2 - 0.68{x_2}^2 - 0.28{x_3}^2 \quad (22)$$

$$y_3 = 50.35 + 18.83x_1 - 1.01x_2 - 2.83x_3 - 1.03x_1x_2 - 0.27x_1x_3 + 0.33x_2x_3 + 4.15{x_1}^2 - 0.48{x_2}^2 + 0.13{x_3}^2 \quad (23)$$

The models $y_1$, $y_2$, and $y_3$ were optimized by removing the non-significant components from the model, as illustrated in equation (24) through (26).

$$y_1 = 1.19 + 1.37x_1 + 0.10x_2 + 0.068x_3 + 0.071x_1x_2 + 0.077x_1x_3 + 0.42{x_1}^2 \quad (24)$$

$$y_2 = 97.50 + 2.16x_1 + 0.35x_3 + 0.41x_1x_2 - 0.78{x_1}^2 - 0.68{x_2}^2 \quad (25)$$

$$y_3 = 50.35 + 18.83x_1 - 2.83x_3 + 4.15{x_1}^2 \quad (26)$$

### 3.3.3. *Two-factor interaction effect analysis*

Within the context of regression equation (21) through (23), the selection of the one-factor level as the midpoint was made arbitrarily to delve into the impact of the remaining two factors upon furrowing power consumption, furrowing depth stability coefficient, and soil cover percentage. Through the application of Design-Expert 12 software for analysis, we obtained response surfaces illustrating the influence of interactive factors, as depicted in Figs. 10–12. In these figures, furrowing depth, forward propulsion velocity, and furrowing blade rotational speed correspond to $x_1$, $x_2$, and $x_3$, respectively.

The order of each factor's influence on furrowing power consumption could be inferred from the aforementioned response surfaces as furrowing depth, forward propulsion velocity, and furrowing blade rotation speed, in that order, decreased.

Fig. 10a showed the interactive effect of furrowing depth and forward propulsion velocity on furrowing power consumption. When moving forward at a constant speed, the power required for furrowing increased rapidly as furrowing depth increased. When the furrowing depth was set at a medium-to-high level, the impact on furrowing power consumption was more noticeable than when it was at a medium-to-low level. This was due to the higher compactness of the soil in deeper layers, requiring the furrowing blades to overcome greater resistance while cutting through the soil. Consequently, this significantly increased furrowing power consumption, as evidenced by the steeper curves in the power consumption graph. This indicated that when the furrowing depth was at a high level, appropriately reducing the furrowing depth could significantly decrease furrowing power consumption. When the furrowing depth was fixed, the consumption of furrowing power rose steadily as the forward propulsion velocity rose.

Fig. 10b showed the interactive effect of furrowing depth and furrowing blade rotation speed on furrowing power consumption. With a constant forward propulsion velocity, the power required for furrowing increased dramatically as furrowing depth increased. With a set furrowing depth, furrowing power consumption increased gradually as the rotation speed of the furrowing blade increased.

Fig. 10c illuminated the dynamic interplay between forward velocity and the rotational speed of the furrowing blade in the context of furrowing power consumption. It was evident that with a constant rotation speed of the furrowing blade, an increment in forward propulsion velocity resulted in a gradual augmentation of furrowing power consumption. When moving at a constant speed, the furrowing power consumption rose progressively as the furrowing blade rotation speed rose. The furrowing power consumption curve changed faster along the forward propulsion velocity '$x_2$' direction than the furrowing blade rotation speed along the '$x_3$' direction, demonstrating that, at the experimental level, furrowing power consumption was more significantly influenced by forward propulsion velocity than by furrowing blade rotation speed.

The hierarchy of each factor's impact upon the furrowing depth stability coefficient could be deduced from the preceding response surfaces, with furrowing depth taking precedence, followed by furrowing blade rotation speed and forward propulsion velocity, in descending order.

Fig. 11d showed the interactive effect of furrowing depth and forward propulsion velocity on furrowing depth stability coefficient. When moving forward at a constant speed, the furrowing depth stability coefficient dramatically rose as the furrowing depth increased. The graph's steeper curves for furrowing depth stability coefficient demonstrated that the impact of furrowing depth on stability

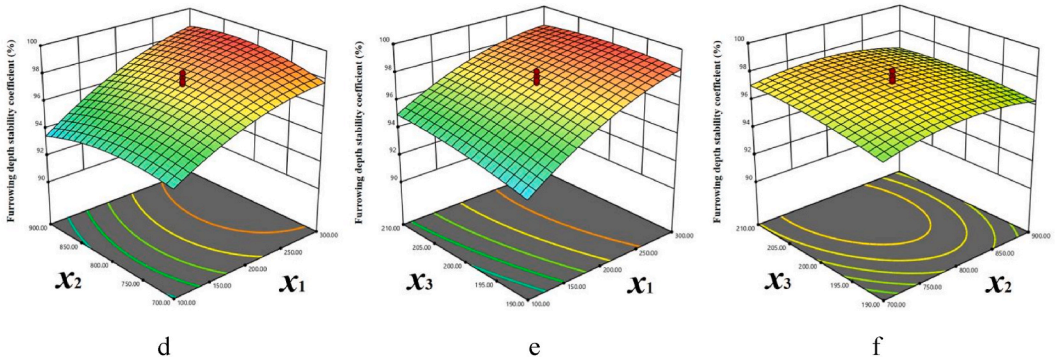


**Fig. 11.** Response surfaces of test factors influence on stability coefficient of furrowing depth.

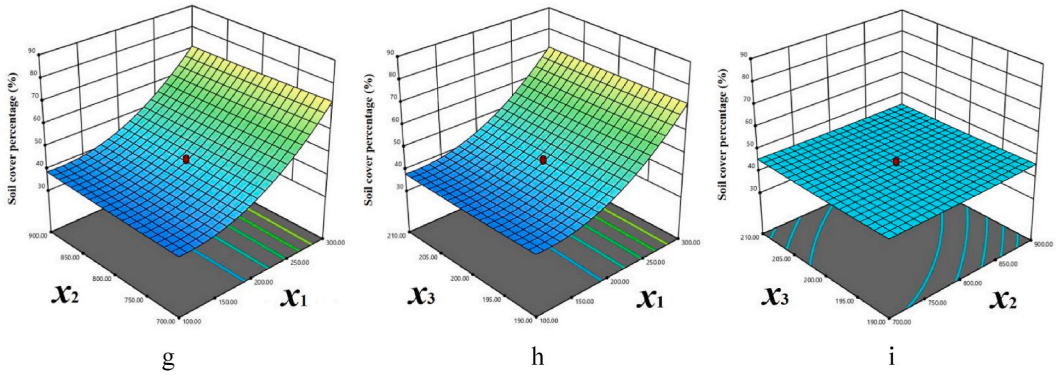


**Fig. 12.** Response surfaces of test parameters influence on uniformity of soil cover percentage.

coefficient was greater when it was at a medium-to-low level than when it was at a medium-to-high level. This was attributed to significant variations in the mechanical properties and stability of the soil within the low-depth range, making it challenging for the furrowing device to maintain stability during operation. As the furrowing depth increased, these variations gradually tended towards stability. This suggested that when the furrowing depth was low, increasing the furrowing depth appropriately could greatly improve the furrowing depth's stability coefficient. With a set furrowing depth, while the forward propulsion velocity increased, the furrowing depth stability coefficient initially rose and subsequently fell.

Fig. 11e displayed the interactive effect of furrowing depth and furrowing blade rotation speed on furrowing depth stability coefficient. When moving forward at a constant speed, the furrowing depth stability coefficient dramatically rose as the furrowing depth increased. When the furrowing depth was fixed, the furrowing depth stability coefficient gradually rose as the furrowing blade's rotation speed rose. The graph's steeper curves for furrowing depth stability coefficient indicated that the impact of the furrowing blade's rotation speed on furrowing depth stability coefficient was greater when it was at a medium-to-low level than when it was at a medium-to-high level. This phenomenon was attributed to the more noticeable shear and lateral displacement effects of the soil at lower furrowing blade rotation speeds, resulting in increased instability. Higher rotation speeds, on the other hand, mitigated instability by altering cutting effects and reducing lateral soil displacement, gradually leading to a stabilized furrowing depth.

Fig. 11f showed how the furrowing depth stability coefficient was affected by the forward propulsion velocity and furrowing blade rotation speed. The stability coefficient of the furrowing depth with a fixed furrowing blade rotation speed first rose and then fell as the forward propulsion velocity rose. At a fixed forward propulsion velocity, the furrowing depth stability coefficient increased gradually as the furrowing blade speed increased.

From the above response surfaces, the order of factors affecting soil cover percentage from high to low was furrowing depth, furrowing blade rotation speed, and forward propulsion velocity.

Fig. 12g showed the interactive effect of furrowing depth and forward propulsion velocity on soil cover percentage. With a constant forward propulsion velocity, the percentage of soil cover rose sharply as furrowing depth increased. The graph's steeper curves for the soil cover percentage indicated that when the furrowing depth was medium to high, it had a greater impact on the soil cover percentage than when it was low to medium. This was because, at lower depths, the soil was more prone to lateral displacement, reducing the amount of soil covering the furrow bottom. With an increase in furrowing depth, the soil cover hood could more effectively collect soil generated along the channel sidewalls, directing it to the furrow bottom and enhancing the soil cover effect. This indicated that when the furrowing depth was at a high level, appropriately increasing the furrowing depth could significantly improve the soil cover percentage. At a constant furrowing depth, the soil cover percentage exhibited a gradual decline as the forward velocity increased.

Fig. 12h displayed the interactive effect of furrowing depth and furrowing blade rotation speed on soil cover percentage. With a constant forward propulsion velocity, the percentage of soil cover rose sharply as furrowing depth increased. At a constant furrowing depth, the soil cover percentage experienced a gradual decline in tandem with an escalation in the rotational speed of the furrowing blade.

Fig. 12i showed how the soil cover percentage was affected by the forward propulsion velocity and furrowing blade rotation speed. With a fixed furrowing blade rotation speed, as the forward propulsion velocity rose, the soil cover percentage steadily declined. In the scenario where the forward propulsion velocity remained unchanging, there was a gradual decline in the soil cover percentage as the rotational speed of the furrowing blade ascended. It is noteworthy that the curve delineating the variations in the soil cover percentage displayed a swifter alteration along the trajectory of the furrowing blade's rotational speed, represented as '$x_3$' in contrast to the '$x_2$' direction, signifying the forward propulsion velocity. This observation underscored that, at the experimental level, the rotational speed of the furrowing blade exerted a more pronounced influence on the soil cover percentage compared to the forward propulsion velocity.

### *3.4. Model optimization and experimental validation*

#### *3.4.1. Parameter optimization*

Attainment of the optimal level of power consumption in the context of orchard furrowing operations, aligned with the agronomic

requisites and the practical exigencies of the orchard trenching fertilizer machine, became imperative. Given the disparate impacts of various factors on the target parameter, a global objective optimization approach was mandated, as established in previous works [23, 24].

The triad of critical parameters governing the furrowing machine, encompassing overall furrowing depth, forward velocity, and blade rotation speed, were subject to meticulous optimization, deploying furrowing power consumption, furrowing depth stability coefficient, and soil cover percentage as the target functions. The mathematical model for the optimization design is explicated as follows:

$$\begin{cases} \min y_1 = (x_1, x_2, x_3) \\ \max y_2 = (x_1, x_2, x_3) \\ \max y_3 = (x_1, x_2, x_3) \\ st. \begin{cases} 0 \le x_1 \le 400 \\ 600 \le x_2 \le 1000 \\ 180 \le x_3 \le 220 \end{cases} \end{cases} \tag{27}$$

To discern the optimal amalgamation of parameters, a comprehensive analysis has been conducted, encompassing three pivotal factors that exert influence upon the realm of furrowing power consumption, furrowing depth stability coefficient, and soil cover percentage, each meticulously fine-tuned for optimization. The optimal operational parameters combination was determined to be: the entire machine's furrowing depth was set to 276.43 mm, forward propulsion velocity was adjusted to 784.15 m/h, and furrowing blade rotation speed was maintained at 190 r/min. Using this optimal parameter combination, discrete element simulation experiments were conducted for furrowing operations, with five repetitions. The averaged results from the simulation experiments were as follows: furrowing power consumption measured 2.35 kW, the furrowing depth stability coefficient reached 98.07%, and the soil cover percentage was recorded at 71.12%.

### *3.4.2. Validation experiment*

A field validation test was executed to corroborate the precision of the regression model and ascertain the optimal combination derived from the parameter optimizations for the orchard trenching fertilizer machine. The experiment employed the 2FQG-2 orchard trenching fertilizer machine, developed by Shandong Agricultural University, which mirrors the structural attributes of the experimental apparatus employed in this investigation.

The test was conducted at the Yifeng Machinery Corporation test facility in Gaomi City, set on a relatively level terrain with loamy soil exhibiting an absolute moisture content of 16.7%. The test area encompassed approximately 650 $m^2$, as depicted in Fig. 13.

For ease of practical application, the optimization parameters were appropriately rounded, setting the whole machine's furrowing depth to 275 mm, the forward propulsion velocity to 785 m/h, and the furrowing blade rotation speed to 190 r/min. Additionally, five reference experiments with different parameter combinations were established to validate the accuracy of the predictive model. The test procedures and metrics were in accordance with GB/T5262—2008, and the test procedures for evaluating the furrowing machinery operation quality were outlined in NY/T740—2003. To ensure the accuracy of the experimental results, each test group underwent three repetitions for averaging. The results for the optimal operational parameter combination were as follows: furrowing power consumption measured 2.39 kW, furrowing depth stability coefficient reached 95.08%, and soil cover percentage was 69.06%. The experimental design and results were presented in Table 7 for reference.

**Fig. 13.** Validation test in field.

**Table 7**
Test metrics field test design and results.

| Serial Number | Furrowing Depth $x_1$/(mm) | Forward Propulsion Velocity $x_2$/(m•h$^{-1}$) | Furrowing Blade Rotation Speed $x_3$/(r•min$^{-1}$) | Furrowing Power Consumption $y_1$/kW | Furrowing Depth Stability Coefficient $y_2$/% | Soil Cover Percentage $y_3$/% |
|---|---|---|---|---|---|---|
| 1 | 100.00 | 700.00 | 190.00 | 0.25 | 90.55 | 32.25 |
| 2 | 150.00 | 750.00 | 195.00 | 0.59 | 92.27 | 35.87 |
| 3 | 200.00 | 800.00 | 200.00 | 1.24 | 94.24 | 43.62 |
| 4 | 250.00 | 850.00 | 205.00 | 2.20 | 95.17 | 53.12 |
| 5 | 300.00 | 900.00 | 210.00 | 3.41 | 96.64 | 70.01 |
| 6 | 275.00 | 785.00 | 190.00 | 2.39 | 95.08 | 69.06 |

The experimental results indicated that, in all six sets of experiments, the relative errors between the measured and predicted values were all below 5%. The close agreement between the measured and predicted values suggested the reliability of the predictive regression model.

## 4. Conclusion

To procure the finest operational parameters for the orchard's furrowing and fertilization machinery, we availed ourselves of a Central Composite experimental design. The independent variables were set as the furrowing depth, forward propulsion velocity, and furrowing blade rotation speed, while the dependent variables were designated as the power consumption during furrowing, furrowing depth stability coefficient, and soil cover percentage. We artfully crafted a multivariate quadratic regression equation to delineate the intricate interplay between the independent variables and their dependent counterparts. A comprehensive analysis of the model's interactions and response surface provided us with valuable insights into the nuanced effects of furrowing depth, forward velocity, and furrowing blade rotation speed on the response indicators.

A model was intricately crafted for the optimization of operational parameters governing the orchard furrowing and fertilization apparatus, culminating in the discernment of an optimal parameter ensemble. Subsequently, when furrowing at a depth of 275 mm, propelling forward at a velocity of 785 m/h, and spinning the furrowing blade at 190 r/min, comprehensive field trials were undertaken to scrutinize these variables. At this time, the furrowing power consumption was 2.39 kW, and the furrowing depth stability coefficient was 95.08%, the soil cover percentage was 69.06%. The results eloquently confirm the reliability of the regression model, as demonstrated by the relative errors between the actual and predicted values, all of which are below the 5% threshold, and the harmonious alignment between the actual and anticipated values. The findings of the study can be utilized as a guide for structural changes to orchard furrowing equipment and the management of furrowing operation parameters.

## Data availability statement

The data are available within the article.

## CRediT authorship contribution statement

**Hongjian Zhang:** Writing – original draft, Writing – review & editing. **Shuai Fan:** Writing – original draft, Writing – review & editing, Conceptualization. **Zixu Chen:** Writing – original draft, Data curation, Conceptualization. **Xin Han:** Conceptualization. **Linlin Sun:** Data curation. **Jingwei Sun:** Methodology. **Guangming Wang:** Methodology. **Shenghui Fu:** Conceptualization. **Chengfu Zhang:** Data curation. **Jinxing Wang:** Writing – review & editing, Funding acquisition. **Shuangxi Liu:** Writing – review & editing, Funding acquisition.

## Declaration of competing interest

We declare that we have no financial and personal relationships with other people or organizations that can inappropriately influence our work, there is no professional or other personal interest of any nature or kind in any product, service and/or company that could be construed as influencing the position presented in, or the review of, the manuscript entitled, 'Targeting optimal power consumption: optimizing operational parameters for orchard furrowing and fertilizing machine'.

## Acknowledgements

This research was funded by the China Agriculture Research System (CARS-27), the Shandong Province Key Research and Development Plan (2022CXGC020706), and the Shandong Province Higher Education 'Youth Innovation Team Plan' Project (2023KJ160).

## References

[1] S. Liu, C. Xu, H. Zhang, H. Jiang, Z. Quan, J. Wang, Research status and development analysis of base-fertilizer application equipment of orchard, Trans. Chin. Soc. Agric. Mach. 51 (2020) 99–108. https://doi:10.6041/j.issn.1000-1298.2020.S2.012.

[2] X. Luo, J. Liao, L. Hu, Y. Zang, Z. Zhou, Improving agricultural mechanization level to promote agricultural sustainable development, Trans. Chin. Soc. Agric. Eng. 32 (2016) 1–11. https://doi:10.11975/j.issn.1002-6819.2016.01.001.
[3] H. Zhang, C. Xu, S. Liu, H. Jiang, C. Zhang, J. Wang, Design and experiment of orchard double row ditching-fertilizer machine with automatic depth adjustment, Trans. Chin. Soc. Agric. Mach. 52 (2021) 62–72. https://doi:10.6041/j.issn.1000-1298.2021.01.007.
[4] H. Xiao, Y. Zhao, W. Ding, S. Hai, Y. Han, Y. Zhang, H. Yan, Z. Song, Design and experiment on blade shaft of 1KS60-35X type orchard double-helix trenching and fertilization machine, Trans. Chin. Soc. Agric. Eng. 33 (10) (2017) 32–39. https://doi:10.11975/j.issn.1002-6819.2017.10.005.
[5] C. Ma, H. Meng, J. Zhang, C. Zhang, Y. Zhao, L. Wang, Research and experiment on the trenching performance of orchard trenching device, Sci. Rep. 13 (2023) 18941, https://doi.org/10.1038/s41598-023-46278-7.
[6] D. Liu, F. Xie, Q. Ye, S. Ren, X. Li, M. Liu, Analysis and experiment on influencing factors on power of ditching parts for 1K-50 orchard ditching, Trans. Chin. Soc. Agric. Eng. 35 (2019) 19–28. https://doi:10.11975/j.issn.1002-6819.2019.18.003.
[7] A. Hasimu, Y. Chen, Soil disturbance and draft force of selected seed openers, Soil Tillage Res. 140 (2014) 48–54, https://doi.org/10.1016/j.still.2014.02.011.
[8] H. Jia, F. Meng, L. Liu, S. Shi, J. Zhao, J. Zhuang, Biomimetic design and experiment of core-share furrow opener, Trans. Chin. Soc. Agric. Mach. 51 (2020) 44–49 77. https://doi:10.6041/j.issn.1000-1298.2020.04.005.
[9] K. Qin, X. Liang, C. Cao, W. Ding, Z. Wu, L. Fang, Design and experiment of combined cutting and throwing ditching blade for tea garden, Trans. Chin. Soc. Agric. Mach. 52 (2021) 74–82. https://doi:10.6041/j.issn.1000-1298.2021.05.008.
[10] S. Wang, S. Li, Y. Zhang, C. Zhang, H. Chen, L. Meng, Design and optimization of inclined helical ditching component for mountain orchard ditcher, Trans. Chin. Soc. Agric. Eng. 34 (2018) 11–22. https://doi:10.11975/j.issn.1002-6819.2018.23.002.
[11] M.A. Sadek, Y. Chen, Z. Zeng, Draft force prediction for a high-speed disc implement using discrete element modelling, Biosyst. Eng. 202 (2021) 133–141, https://doi.org/10.1016/j.biosystemseng.2020.12.009.
[12] M.A. Matin, J.M. Fielke, J.M.A. Desbiolles, Torque and energy characteristics for strip-tillage cultivation when cutting furrows using three designs of rotary blade, Biosyst. Eng. 129 (2015) 329–340, https://doi.org/10.1016/j.biosystemseng.2014.11.008.
[13] J.B. Barr, J.M.A. Desbiolles, J.M. Fielke, Minimising soil disturbance and reaction forces for high speed sowing using bentleg furrow openers, Biosyst. Eng. 151 (2016) 53–64, https://doi.org/10.1016/j.biosystemseng.2016.08.025.
[14] C. Ma, J. Qi, Z. Kan, S. Chen, H. Meng, Operation power consumption and verification tests of a trenching device for orchards in Xinjiang based on discrete element, Int. J. Agric. Biol. Eng. 14 (2021) 133–141. https://doi:10.25165/j.ijabe.20211401.5477.
[15] J. Kang, S. Li, X. Yang, L. Liu, C. Li, Experimental verification and simulation analysis on power consumption of disc type ditcher, Trans. Chin. Soc. Agric. Eng. 32 (2016) 8–15. https://doi:10.11975/i.issn.1002-6819.2016.13.002.
[16] J. Xia, X. He, S. Yu, Y. Zhou, Finite element simulation of soil cutting with rotary knife roller based on ANSYS/LS-DYNA software, Trans. Chin. Soc. Agric. Eng. 29 (2013) 34–41+293. https://doi:10.3969/j.issn.1002-6819.2013.10.005.
[17] K. Tamás, The role of bond and damping in the discrete element model of soil-sweep interaction, Biosyst. Eng. 169 (2018) 57–70, https://doi.org/10.1016/j.biosystemseng.2018.02.001.
[18] J. Hu, J. Zhao, H. Pan, W. Liu, X. Zhao, Prediction model of double axis rotary power consumption based on discrete element method, Trans. Chin. Soc. Agric. Mach. 51 (2020) 9–16. https://doi:10.6041/j.issn.1000-1298.2020.S1.002.
[19] J. Lin, T. Ma, B. Li, Design and test of 1JHL-2 type straw deep burying and returning machine, Trans. Chin. Soc. Agric. Eng. 33 (20) (2017) 32–40. https://doi:10.11975/j.issn.1002-6819.2017.20.004.
[20] G. Wu, W. Fu, J. Dong, Y. Cong, Z. Meng, Design and experiment of 1KY-40 hydraulic drive ditcher for farmland conduit, Trans. Chin. Soc. Agric. Mach. 45 (2014) 302–308. https://doi:10.6041/j.issn.1000-1298.2014.S0.049.
[21] K. Zheng, J. He, H. Li, P. Diao, Q. Wang, H. Zhao, Research on polyline soil-breaking blade subsoiler based on subsoiling soil model using discrete element method, Trans. Chin. Soc. Agric. Mach. 47 (2016) 62–72, https://doi.org/10.6041/j.issn.1000-1298.2016.09.010.
[22] J. Lu, Q. Shang, Y. Yang, Z. Li, J. Li, Z. Liu, Design optimization and experiment on potato haulm cutter, Trans. Chin. Soc. Agric. Mach. 47 (2016) 106–114+198. https://doi:10.6041/j.issn.1000-1298.2016.05.015.
[23] C. Cheng, J. Fu, Z. Chen, F. Hao, S. Cui, L. Ren, Optimization experiment on cleaning device parameters of corn kernel harvester, Trans. Chin. Soc. Agric. Mach. 50 (2019) 151–158. https://doi:10.6041/j.issn.1000-1298.2019.07.015.
[24] W. Zheng, Z. Lu, W. Zhang, Z. Liu, Y. Lu, Y. Li, Design and test of single row sweet potato vine recycling machine, Trans. Chin. Soc. Agric. Eng. 35 (2019) 1–9. https://doi:10.11975/j.issn.1002-6819.2019.06.001.
[25] X. Luo, J. Liao, X. Zou, Z. Zhang, Z. Zhou, Y. Zang, L. Hu, Enhancing agricultural mechanization level through information technology, Trans. Chin. Soc. Agric. Eng. 32 (2016) 1–14. https://doi:10.11975/j.issn.1002-6819.2016.20.001.
[26] X. Wang, B. Yue, X. Gao, Z. Zheng, R. Zhu, Y. Huang, Discrete element simulations and experiments of disturbance behavior as affected by mounting height of subsoil's wing, Trans. Chin. Soc. Agric. Mach. 49 (2018) 124–136. https://doi:10.6041/j.issn.1000-1298.2018.10.014.
[27] H. Lin, J. He, H. Li, H. Li, Q. Wang, C. Lu, Y. Li, S. Jiang, A review of research progress on soil organic cover machinery in china, Agriculture 12 (9) (2022) 1311. https://doi:10.3390/agriculture12091311.